



FEAST: JWST/NIRCam View of the Resolved Stellar Populations of the Interacting Dwarf Galaxies NGC 4485 and NGC 4490

Giacomo Bortolini¹ , Matteo Correnti^{2,3} , Angela Adamo¹ , Michele Cignoni^{4,5,6} , Elena Sacchi⁷ , Monica Tosi⁵ , Göran Östlin¹ , Anastasios Kapodistrias^{1,8} , Arjan Bik¹ , Daniela Calzetti⁹ , Ana Duarte-Cabral¹⁰ , Flavia Dell’Aglì² , John S. Gallagher¹¹ , Benjamin Gregg⁹ , Kathryn Grasha^{12,13,21} , Thomas S.-Y. Lai¹⁴ , Drew Lapeer⁹ , Sean T. Linden¹⁵ , Matteo MESSA⁵ , Alex Pedrini¹ , Elena Sabbi^{16,17} , Linda J. Smith¹⁶ , Helena Faustino Vieira¹ , John M. Cannon¹⁸ , Salvador Duarte Puertas¹⁹ , and Carmelle Robert²⁰

¹ Department of Astronomy, The Oskar Klein Centre, Stockholm University, AlbaNova, SE-10691 Stockholm, Sweden; giacomo.bortolini@astro.su.se

² INAF Osservatorio Astronomico di Roma, Via Frascati 33, 00078 Monteporzio Catone, Rome, Italy

³ ASI-Space Science Data Center, Via del Politecnico, I-00133 Rome, Italy

⁴ Dipartimento di Fisica, Università di Pisa, Largo Bruno Pontecorvo 3, 56127 Pisa, Italy

⁵ INAF—Osservatorio di Astrofisica e Scienza dello Spazio di Bologna, via Piero Gobetti 93/3, 40129 Bologna, Italy

⁶ INFN, Largo B. Pontecorvo 3, 56127 Pisa, Italy

⁷ Leibniz-Institut für Astrophysik Potsdam (AIP), An der Sternwarte 16, 14482 Potsdam, Germany

⁸ Department of Teaching & Learning, Stockholm University, Svante Arrhenius väg 20 A, 10691 Stockholm, Sweden

⁹ Department of Astronomy, University of Massachusetts, 710 North Pleasant Street, Amherst, MA 01003, USA

¹⁰ Cardiff Hub for Astrophysics Research and Technology (CHART), School of Physics & Astronomy, Cardiff University, The Parade, Cardiff CF24 3AA, UK

¹¹ Department of Astronomy, University of Wisconsin-Madison, 475 North Charter Street, Madison, WI 53706, USA

¹² Research School of Astronomy and Astrophysics, Australian National University, Canberra, ACT 2611, Australia

¹³ ARC Centre of Excellence for All Sky Astrophysics in 3 Dimensions (ASTRO 3D), Australia

¹⁴ IPAC, California Institute of Technology, 1200 East California Boulevard, Pasadena, CA 91125, USA

¹⁵ Steward Observatory, University of Arizona, 933 North Cherry Avenue, Tucson, AZ 85719, USA

¹⁶ Space Telescope Science Institute, 3700 San Martin Drive, Baltimore, MD 21218, USA

¹⁷ Gemini Observatory/NSF’s NOIRLab, 950 North Cherry Avenue, Tucson, AZ 85719, USA

¹⁸ Macalester College, 1600 Grand Avenue, Saint Paul, MN 55105, USA

¹⁹ Departamento de Física Teórica y del Cosmos, Campus de Fuentenueva, Edificio Mecenaz, Universidad de Granada, E-18071 Granada, Spain

²⁰ Université Laval & Centre de recherche en astrophysique du Québec, Québec, QC, Canada

Received 2025 July 7; revised 2025 August 15; accepted 2025 August 17; published 2025 September 30

Abstract

We present new JWST/NIRCam observations of the interacting dwarf galaxy system NGC 4485–NGC 4490 (aka Arp 269), obtained as part of the Cycle 1 Feedback in Emerging Extragalactic Star Clusters (FEAST) program. NGC 4485 and NGC 4490 form the closest known pair of interacting late-type dwarf galaxies (at ~ 7.4 Mpc), excluding the Magellanic Clouds. Near-infrared color–magnitude diagrams (CMDs) reveal a wide range of stellar populations in both galaxies, including young ($\lesssim 200$ Myr) upper main-sequence stars, core helium-burning stars, and oxygen-rich asymptotic giant branch (AGB) stars. We also identify intermediate-age (~ 200 Myr–1 Gyr) carbon-rich AGB stars and a well-populated old ($\gtrsim 1$ Gyr) red giant branch. The CMDs show two distinct bursts of star formation beginning ~ 30 and ~ 200 Myr ago, the latter consistent with the most recent pericenter passage predicted by N -body simulations. The spatial distribution of stars reveals a tidal bridge extending from NGC 4485 and connecting to the disk of NGC 4490. Compact star-forming regions are seen along NGC 4490’s spiral arms, possibly originating from its infrared nucleus. A significant metallicity gradient is observed in the young stellar populations forming the bridge. These findings suggest that during the last pericenter passage, gas was stripped from NGC 4485 via tidal forces or ram pressure, accreted by NGC 4490, and mixed with in situ material, fueling ongoing star formation. This system provides a unique nearby laboratory for studying how tidal interactions shape the star formation and chemical enrichment history of dwarf galaxies.

Unified Astronomy Thesaurus concepts: Dwarf galaxies (416); Star formation (1569); Galaxy interactions (600); Galaxy stellar content (621)

1. Introduction

The Λ cold dark matter cosmological model is quite successful at reproducing most of the observed properties of our Universe (S. D. M. White & M. J. Rees 1978; P. J. E. Peebles 1982; C. S. Frenk et al. 1988; S. D. M. White & C. S. Frenk 1991), but still faces some observational challenges

(S. Tulin & H.-B. Yu 2018). Among these, we highlight the prediction that present-day dwarf galaxies should be surrounded by a large population of satellites and stellar streams (e.g., J. Diemand et al. 2008; C. Wheeler et al. 2015), a property not sufficiently verified by observations yet (A. V. Kravtsov et al. 2004; J. D. Simon & M. Geha 2007). While the interaction of satellites with massive galaxies has been vastly confirmed by observations of spirals and giant ellipticals in the Local Volume (e.g., R. Ibata et al. 2001; V. Belokurov et al. 2006; A. W. McConnachie et al. 2009; D. Martínez-Delgado et al. 2010; D. Crnojević et al. 2016), robust statistics on the satellites of dwarf galaxies and on their interactions is still missing (e.g., F. Annibali & M. Tosi 2022, and references therein), except

²¹ ARC DECRA Fellow.



for a few interesting and well-studied cases. For instance, there is clear evidence that the Magellanic Clouds have several satellites and interaction debris (e.g., V. Belokurov et al. 2017; N. Kallivayalil et al. 2018; S. A. Pardy et al. 2020; E. Patel et al. 2020), and that other late-type dwarfs have many tidal features or satellites (e.g., M. Hancock et al. 2009; G. Bortolini et al. 2024a; E. Sacchi et al. 2024; L.-Y. Zhang et al. 2024; R. Garner et al. 2025), even when located in huge voids (e.g., DDO 68; Y. I. Izotov & T. X. Thuan 2009; N. A. Tikhonov et al. 2014; F. Annibali et al. 2016, 2023; M. Correnti et al. 2025a).

Studying interactions or accretions of satellite systems is not only a valuable testing ground for cosmological models, but is also key to understand how they impact the evolution of galaxies, affecting their morphology and kinematics, and providing mechanisms to trigger gas flows and starbursts (I. D. Karachentsev et al. 2018). In turn, understanding how exactly interactions and accretions affect the evolution of local galaxies is the only means to figure out how high-redshift and primordial galaxies may have evolved in the early Universe.

Obtaining reliable statistics on the fraction of satellites and streams around dwarf galaxies is challenging because these systems, with their satellites and/or merger signatures, often have extremely low surface brightness and are difficult to detect. However, in the last decade an increasing effort is being invested in surveys specifically devoted to the search for small satellites around dwarf systems. Several ground-based, wide-field, photometric surveys are currently underway: the Solitary Local dwarfs survey, targeting 42 isolated dwarf galaxies within 3 Mpc of the Milky Way (C. R. Higgs et al. 2016); the Magellanic Analog Dwarf Companions and Stellar Halos, designed to use resolved stars to map the virial volumes of galaxies within $\lesssim 4$ Mpc and with stellar masses of $1\text{--}7 \times 10^9 M_\odot$ (J. L. Carlin et al. 2016); and the Smallest Scale Hierarchy survey (F. Annibali et al. 2020), designed to determine the frequency and properties of interaction and merging events around a sample of 45 late-type dwarfs at distances between ~ 1 and ~ 10 Mpc, with the aim of revealing the presence of faint tidal features around them down to a surface brightness of $\mu_r \simeq 31$ mag arcsec $^{-2}$. The formation history and stellar populations of candidate satellites and streams can be studied in detail in the optical and near-infrared (NIR) thanks to the exceptional sensitivity and spatial resolution of space telescopes like the Hubble Space Telescope (HST) and the James Webb Space Telescope (JWST), which can resolve individual stars and star clusters in targets within approximately 20 Mpc (see E. Tolstoy et al. 2009; F. Annibali & M. Tosi 2022, for in-depth reviews).

In this context, we present here the interesting case of the interacting system NGC 4485–NGC 4490 (aka Arp 269), located at an average distance of ~ 7.4 Mpc (D. Calzetti et al. 2015; E. Sabbi et al. 2018), one of the closest known double dwarf colliding systems (S. Pearson et al. 2018). This pair of galaxies is one of the targets of the cycle 1 JWST program Feedback in Emerging Extragalactic Star Clusters (FEAST; PI: A. Adamo). The galaxies are separated by only ~ 7.5 kpc in projection, with a prograde motion and a velocity separation of ~ 30 km s $^{-1}$ (S. Pearson et al. 2018). The closest massive galaxy to the pair is NGC 4369 ($M_\star = 2.6 \times 10^{10} M_\odot$), at a projected distance of 310 kpc (S. Pearson et al. 2018). NGC 4490 is a low-luminosity late-type galaxy, imaged by the HST within the Treasury program LEGUS (D. Calzetti et al. 2015) and classified there as SBd with a stellar mass of

$\sim 2.5 \times 10^9 M_\odot$, a star formation rate (SFR) inferred from the far-ultraviolet of $2.8 M_\odot \text{ yr}^{-1}$ (D. Calzetti et al. 2015), and an oxygen abundance derived from H II region emission lines of $12 + \log(\text{O}/\text{H}) = 8.37$ (L. S. Pilyugin & T. X. Thuan 2007). NGC 4485, also observed by LEGUS with HST, is classified as IBm, with a mass an order of magnitude lower than its companion ($M \sim 3.2 \times 10^8 M_\odot$), a low recent SFR of $\sim 0.2 M_\odot \text{ yr}^{-1}$, and no information on its chemical abundance. Interestingly, the stellar mass and metallicity of NGC 4490 are fairly similar to those of our closest late-type satellite, the Large Magellanic Cloud (K. Bekki & M. Chiba 2005), and the ratio of stellar masses of the two members ($\sim 8:1$; M. S. Clemens et al. 1998) is also similar to that of the two Magellanic Clouds. Moreover, HST imaging from the LEGUS survey confirmed the presence of a faint bridge that may connect the two galaxies, a structure first identified by D. M. Elmegreen et al. (1998). This feature corresponds to some bright star-forming regions, as observed by H. A. Thronson et al. (1989) in H α and GALEX in the UV (B. J. Smith et al. 2010). H I and CO (1–0) emission in the bridge region has been detected using preliminary Very Large Array (VLA; J. Cannon et al. 2025, private communication) and IRAM 30 m telescope observations (S. Linden 2025, private communication), further suggesting the presence of dense gas in this extended tidal structure. We are therefore dealing with an intriguing analog of the Magellanic Cloud system (L. T. Gardiner & M. Noguchi 1996; K. Bekki & M. Chiba 2005; G. Besla et al. 2010; M. Guglielmo et al. 2014; S. A. Pardy et al. 2018), with the important difference that our targets are not affected by the presence of a more massive companion like the Milky Way.

Despite the wealth of observations, the system’s interaction history remains elusive. Some authors propose that NGC 4490 is a relatively young galaxy, approximately 2 Gyr old, undergoing continuous star formation at a steady rate for at least the past 100 Myr (D. M. Elmegreen et al. 1998; M. S. Clemens et al. 1999, 2000). In this scenario, the two galaxies would have interacted only once, with their closest approach occurring around 100 Myr ago. In contrast, recent N -body and test-particle simulations by S. Pearson et al. (2018) suggest that the galaxies have experienced two encounters, with perigalactic passages taking place approximately 1.3 Gyr and 230 Myr ago. To complicate the picture even more, A. Lawrence et al. (2020) recently found that NGC 4490 has a double nucleus morphology, with one nucleus visible in the optical and one only in the infrared (IR; see Figure 3 of A. Lawrence et al. 2020). Due to their mass and luminosity being comparable to other nuclei found in interacting galaxy pairs, the authors argued that NGC 4490 might be itself a merger remnant, which is now further interacting with NGC 4485. Finally, recent observations with the Five-hundred-meter Aperture Spherical radio Telescope revealed an impressive H I tidal tail extending approximately 100 kpc both to the south and north (Y. Liu et al. 2023), indicating a highly complex and extended dynamical environment (I. D. Karachentsev & P. Kroupa 2024).

In this paper, we focus on the properties of the resolved stellar populations of NGC 4485, NGC 4490, and their bridge, based on our deep NIRC2 imaging and analysis of NIR color–magnitude diagrams (CMDs). Our goal is to shed light on the complex interaction history of this system. A more detailed study of its star formation history, based on the synthetic CMD method, is currently in preparation

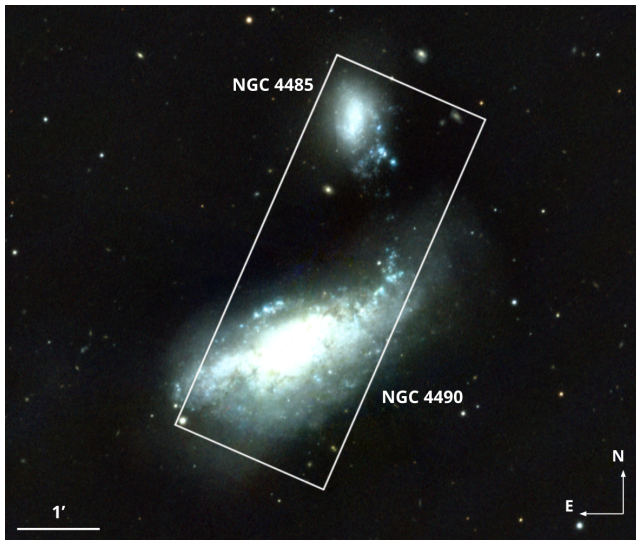


Figure 1. Footprint for the FEAST JWST/NIRCam mosaic of NGC 4485 and NGC 4490 (white rectangle) overlaid upon an optical-band image adopted from the Panoramic Survey Telescope and Rapid Response System (K. C. Chambers et al. 2016). The two dwarf galaxies are labeled. North is up, east is to the left.

(G. Bortolini et al. 2025, in preparation). The paper is organized in three main sections. In Section 2 we describe in detail our JWST data, reduction pipeline, point-spread function (PSF) fitting photometry and artificial stars test routine. In Section 3 we present our analysis of the NGC 4485 and NGC 4490 CMDs, the properties of their different stellar populations, and their spatial distributions within the system. Finally, in Section 4 we summarize our results.

2. Observations and Data Reduction

We present JWST observations of the NGC 4485–NGC 4490 system, carried out as part of the Cycle 1 program FEAST (PI: A. Adamo). In particular, the target was imaged by NIRCam (M. J. Rieke et al. 2023) with a combination of narrow-, medium-, and wide-band filters (i.e., F187N, F115W, F150W, F200W, F300M, F335M, F405N, and F444W), and by MIRI (G. H. Rieke et al. 2015) in the F560W and F770W filters. The NIRCam mosaics (footprint shown in Figure 1) have been observed with a FULLBOX 4TIGHT primary dither pattern, along with two small dithers resulting in eight single exposures covering $6'.0 \times 2'.2$ when combined. For the purpose of this study, we focus solely on the NIRCam’s F115W and F200W filters. Among all the NIR short-wavelength filters available, this combination offers the best trade-off between high resolution and depth, allowing us to probe and resolve the galaxies’ stellar populations, even in the crowded fields of their central regions. We note that the F200W filter includes the Pa α recombination line. Nevertheless its presence has negligible effect on the stellar photometry. We refer the reader to A. Adamo et al. (2025, in preparation) for an in-depth overview of the FEAST survey.

Figure 2 shows a color composite image of the NIRCam mosaic of NGC 4485 and NGC 4490, with the F115W and F200W filters in blue and green, respectively, tracing the stellar continuum, and the F444W filter in red tracing the dust reemission in the NIR of UV photons from massive stars in young star-forming regions. This emission follows the spiral arms, as seen in optical images, and seems to be centered on

the IR nucleus (black star; A. Lawrence et al. 2020). We also report the presence of a series of red and bright H II regions, forming a striking bridge from the southwest to the northeast side of the image, connecting the two dwarfs’ main bodies dominated by the blue stellar continuum.

2.1. Stellar Photometry

We performed PSF fitting photometry on both the F115W and F200W images simultaneously, using the latest version of the software package DOLPHOT 2.0 (A. E. Dolphin 2000; A. Dolphin 2016) NIRCam module (D. R. Weisz et al. 2024). We used the F200W drizzled `*i2d.fits` image, aligned to Gaia Data Release 3 (Gaia Collaboration et al. 2023) as an astrometric reference, while the actual photometry was performed on the individual `*crf.fits` images. The `*.fits` files have been processed using the pipeline versions CAL VER = 1.11.3, CRDS VER = 11.16.20, and CRDS CTX = jwst 1100.pmap. We ran the photometry following the prescriptions suggested in D. R. Weisz et al. (2024). The final magnitudes are calibrated in the Vega system, using updated zero-points aligned with the recommended Sirius–Vega-based calibration system (D. R. Weisz et al. 2024).

Due to the large field of view covered by our observations and the extremely high number of measured point sources, we ran DOLPHOT on 18 similarly sized portions of the reference image (hereafter referred to as tiles; see Figure 2) to speed up the reduction process, and the artificial star tests (ASTs; see Section 2.2). Each of the 18 “raw” photometric catalogs were inspected and culled to remove as many interlopers as possible (i.e., background galaxies, blends, and spurious detections) while retaining the largest number of bona fide stars. To do so, we exploit several diagnostic parameters given by DOLPHOT.²² We first required `Object_Type < 1`, `quality_flag ≤ 2`, and `SNR > 2`. We then applied further “bell-shaped” selections cuts on the parameters `sharpness` and `crowding`, using the same prescriptions described in M. Correnti et al. (2025b). The sharpness selection was based on the distribution of sharpness versus magnitude. We included sources with `|sharpness| < 0.075` or those lying within $\pm 2\sigma$ of the local mean. For the crowding parameter, we selected sources with `crowding < 0.1`, or alternatively, those within 3σ of the local mean.

2.2. Artificial Star Tests

ASTs are essential in photometric studies of crowded fields, providing the most robust and consistent method for estimating uncertainties and completeness as a function of a star’s magnitude, color, and position in the image (M. Cignoni et al. 2016; D. R. Weisz et al. 2024). Taking advantage of our tiled photometry approach, we injected one million artificial stars in each tile (for a total of 18 million artificial stars), spatially distributed to mimic the light profile of the image, and cover uniformly the magnitude range (16, 30) and color range (−2, 4) of our data. Each artificial star was injected separately in each tile, in order not to bias our completeness estimation. Photometry was then carried out using the same DOLPHOT parameters as in the original run, and the output catalogs filtered using the same selection cuts described in Section 2.1. An input artificial star that is detected and that passes the

²² See the DOLPHOT manual at <http://americano.dolphinim.com/dolphot/> for an in-depth description of the output parameters.

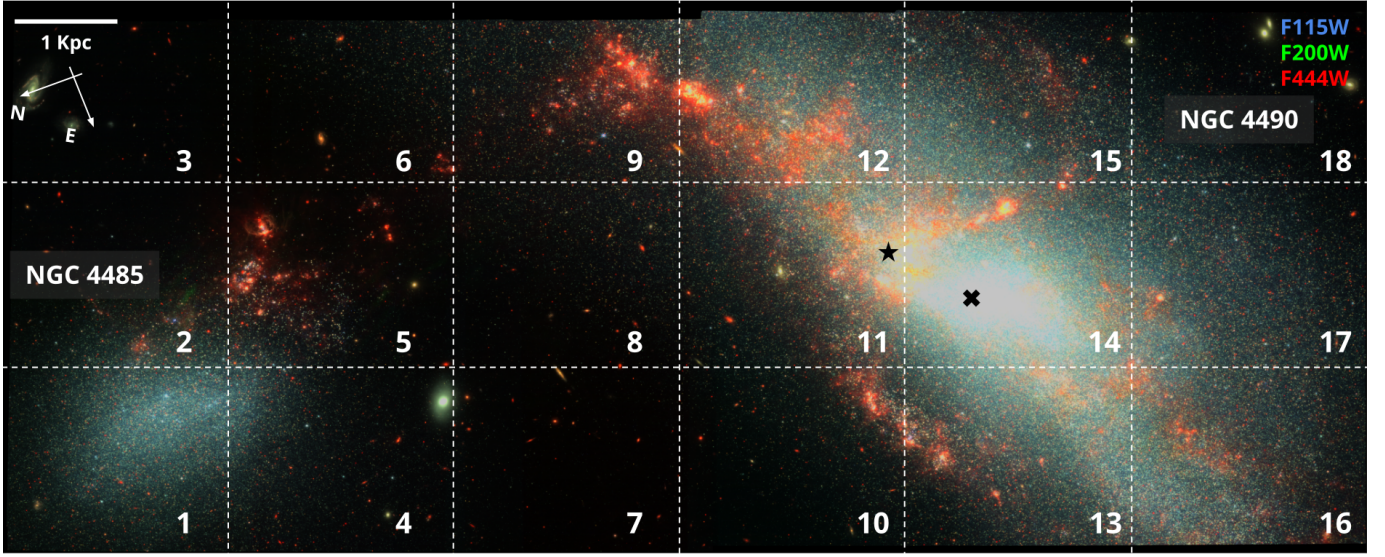


Figure 2. Color composite image of NGC 4485 and NGC 4490, constructed by combining the NIRCcam observations obtained as part of the FEAST program in F115W (blue channel), F200W (green channel), and F444W (red channel). The field of view is divided into 18 tiles, which are outlined with dashed white lines and numbered from left to right, and bottom to top. The F115W and F200W trace the stellar continuum, while dust emission from star-forming regions shines in the F444W. The two dwarf galaxies are labeled. The black cross and star symbols mark the respective positions of the optical and IR nuclei (A. Lawrence et al. 2020). Particularly bright background galaxies can also be identified in tiles 3, 4, 6, and 18.

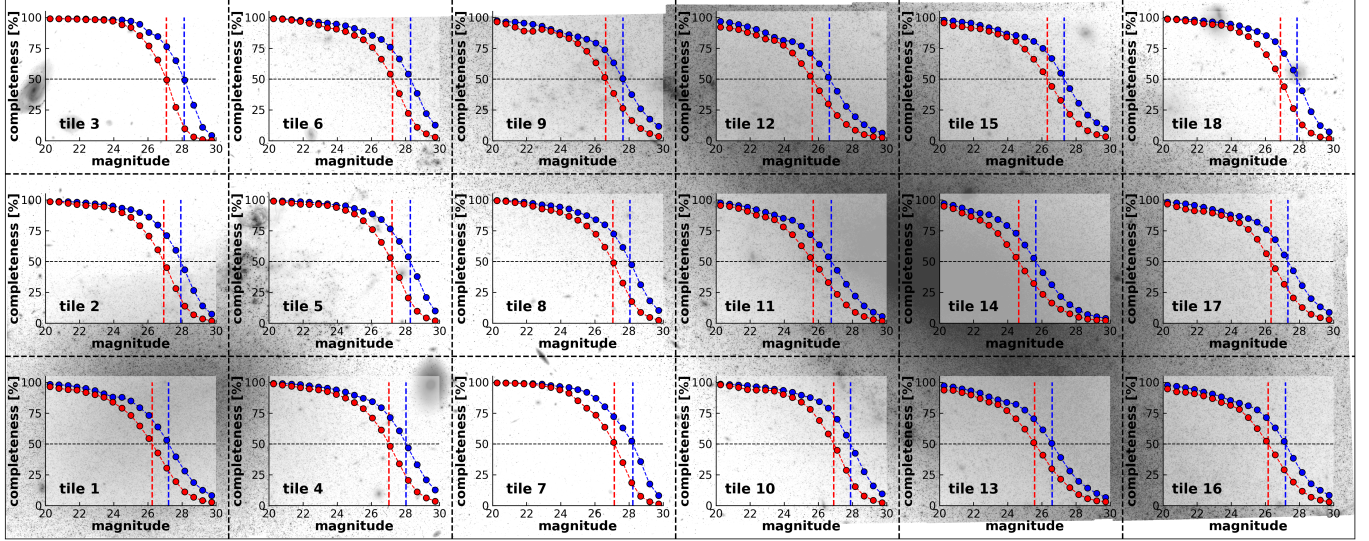


Figure 3. NIRCcam F200W image, with superimposed for each tile the completeness of the photometry as a function of magnitude, derived from our ASTs, in both the F115W (blue) and F200W (red) filters. The 50% completeness level is marked by the dashed gray line, while the magnitude at which this limit is reached in each filter is marked by the dashed vertical lines.

quality cuts is considered a recovered star. We can estimate the photometric errors of a star as a function of its color and magnitude from the distribution of the difference between the output and input magnitudes, while the completeness can be evaluated taking the ratio between the number of recovered and injected artificial stars.

Figure 3 shows the color-averaged photometric completeness as a function of input magnitude and position in the image (i.e., for each tile), in both the F115W (blue dots) and F200W (red dots) filters. The completeness levels are displayed on top of the F200W reference image. In each subplot, the 50% completeness level is marked by a dashed gray line, while the magnitude at which it is reached in each filter is marked by the

dashed vertical lines. The 50% completeness level is reached around $m_{\text{F115W}} = 27$ mag and $m_{\text{F200W}} = 26$ mag in the central part of NGC 4485, while it is ~ 1 mag shallower in the more crowded center of NGC 4490.

3. Resolved Stellar Population Analysis

3.1. Color–Magnitude Diagrams

Figure 4 shows the m_{F200W} versus $m_{\text{F115W}} - m_{\text{F200W}}$ CMDs overplotted on the positions of the respective tiles, after we apply the quality cuts presented in Section 2.1. To help the reader’s eye in exploring the different stellar populations present in the diagrams, the high-density regions have been

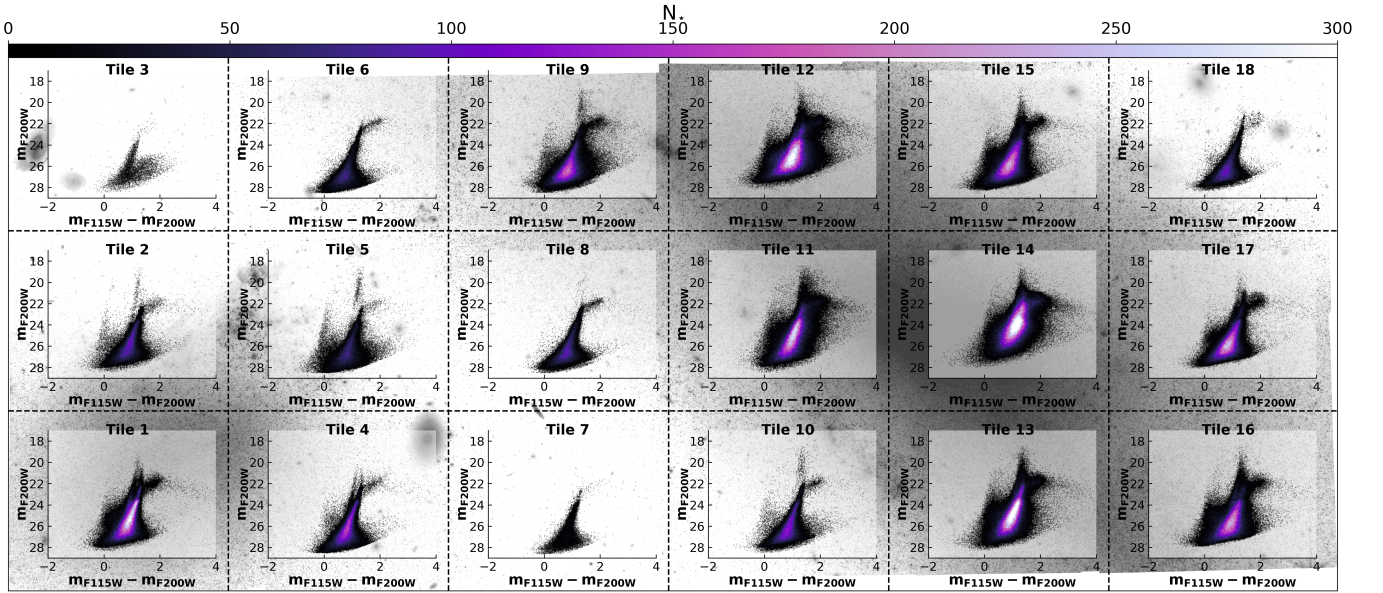


Figure 4. m_{F200W} vs. $m_{F115W} - m_{F200W}$ CMDs for each tile, displayed on top of the F200W reference image of the NGC 4485–NGC 4490 system. The high-density regions of the CMDs have been binned and color coded according to the number of stars in each bin (see color bar on the top).

binned and color coded based on stellar density. At first glance, a wide range of stellar populations are immediately visible, with the CMDs exhibiting different shapes and sizes across the two galaxies and even from tile to tile. The main features, in most of the tiles, include a bright-blue vertical sequence at $m_{F115W} - m_{F200W} \sim 0$ mag composed of young upper main-sequence (MS) stars and more evolved core He-burning stars at the blue edge of their loops, i.e., the so-called blue loop (BL) phase. Some examples can be seen in tiles 1, 2, 5, 9, 10, 12, 15, and 16. A distinct red vertical sequence is present at $m_{F115W} - m_{F200W} \sim 1$ mag and $m_{F200W} \lesssim 23$ mag, composed of massive ($8 M_{\odot} \lesssim M \lesssim 25 M_{\odot}$) core He-burning stars, but this time on the red edge of their loops, also known as the red supergiant (RSG) phase. Strong examples of this phase appear to be in tiles 2, 5, 9, and 10, which are tiles that clearly show young H II regions based on the JWST imaging in Figure 2. This stellar evolutionary phase occurs in the life of bright massive stars and is characterized by a strong anticorrelation between the stars’ ages and luminosities (i.e., the luminosity decreases with increasing age; e.g., A. Maeder & G. Meynet 2001, A. Bressan et al. 2012). All these properties make these stars particularly well suited to be used as “astronomical clocks” in distant galaxies (see among others R. C. Dohm-Palmer et al. 1997; E. Sacchi et al. 2016). In between these two sequences, we observe a sparse cloud of young He-burning stars, in the process of going from the red to the blue edge (and vice versa) of their loops. A red “finger,” running almost parallel to the RSG sequence around $m_{F115W} - m_{F200W} \sim 1.25$ mag and $m_{F200W} \sim 21$ mag, is also present in some tiles (e.g., tiles 1 and 4). This region of the CMD is mainly populated by intermediate-mass ($4 M_{\odot} \lesssim M \lesssim 8 M_{\odot}$) oxygen-rich asymptotic giant branch (AGB) stars. A distinct group resembling a red “tail” is present at $m_{F115W} - m_{F200W} \sim 2$ mag and $m_{F200W} \sim 22$ mag, primarily consisting of less massive ($1.2 M_{\odot} \lesssim M \lesssim 4 M_{\odot}$) AGB stars in their thermally pulsing (TP) phase. During this phase, inner-shell convective episodes, known as the third dredge-up, transport a substantial amount of carbon to the stellar surface.

This carbon is then released into the interstellar medium (ISM) through strong winds that produce mainly carbon dust (A. Nanni et al. 2013; P. Ventura et al. 2014), causing these stars to appear redder compared to their O-rich counterparts. As a result, these stars are also referred to as carbon-rich AGB stars. Last but not least, low-mass ($M \lesssim 1.0 M_{\odot}$) red giant branch (RGB) stars dominate the entire region of the diagrams around $m_{F115W} - m_{F200W} \sim 1$ mag, going from our faintest detection limit at $m_{F200W} \sim 28$ mag, up to their tip located at $m_{F200W} \sim 23.8$ mag.

Figure 5 presents zoom-in views of the CMDs of tile 1 (left panel) and tile 5 (right panel), with some of the main features discussed above highlighted and labeled. In tile 1, these include the O-rich AGB “finger,” the C-rich AGB red “tail,” the RGB sequence, and an overdensity of blue He-burning stars. In tile 5, a gap in the RSG sequence is marked, together with the MS plus BL star blue sequence. These and other features will be analyzed in more detail in the next section, through comparisons with PARSEC–COLIBRI stellar isochrones.

3.2. Isochrone Comparison

Figure 6 shows the CMDs for tiles 1 and 5, which cover the main body of NGC 4485 and part of the bridge, respectively, as well as tiles 9, 10, 12, and 14, which sample the remaining portion of the bridge and regions of particular interest within NGC 4490. To more easily identify the different stellar populations present, we plotted a set of PARSEC–COLIBRI isochrones (A. Bressan et al. 2012; P. Marigo et al. 2017; G. Pastorelli et al. 2020), assuming a distance modulus of $(m - M)_0 = 29.70$ (D. Calzetti et al. 2015; E. Sabbi et al. 2018) and a color excess of $E(B - V) = 0.15$ (E. Sabbi et al. 2018). We could not anticipate any substantial difference in the distances of the two dwarfs in our study, but an in-depth analysis using the tip of the RGB method (e.g., M. G. Lee et al. 1993; M. Salaris & S. Cassisi 1998; M. Bellazzini et al. 2004; D. Makarov et al. 2006; M. Bellazzini & R. Pascuale 2024, and references therein) is beyond the scope of this

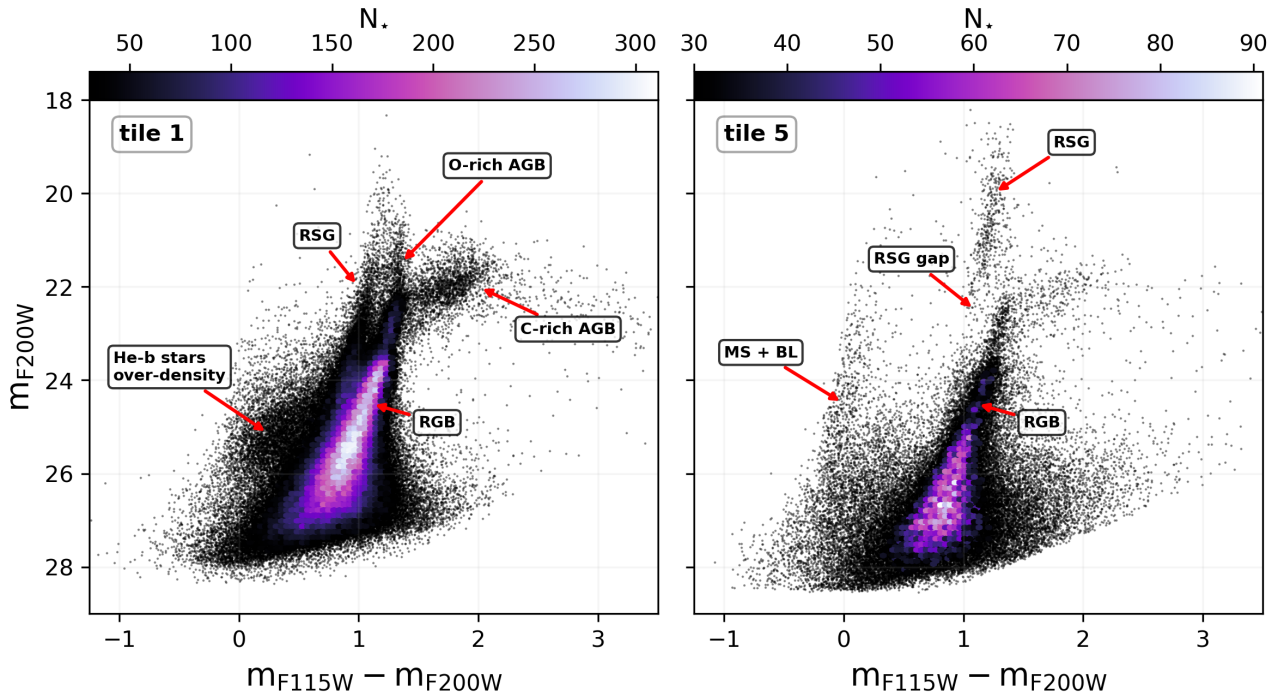


Figure 5. Zoom-in views of the CMDs of tile 1 (left panel) and tile 5 (right panel), with some of the features discussed in Sections 3.1 and 3.2 highlighted and labeled accordingly. The high-density regions in the diagrams are binned and color coded, ranging from black to white according to the number of stars in each bin.

paper. The isochrones are color coded according to their age and metallicity (see the legend on the right-hand side of each panel). The TPAGB phase in the isochrones is shown with a lower opacity, due to the intrinsic uncertainties affecting the modeling of this particular stellar phase (P. Ventura et al. 2018). Error bars on the left-hand side of the plots are the photometric errors as a function of magnitude, estimated via the extensive ASTs (see Section 2.2). Finally, the shaded area marks the portion of the CMDs that lie below the 50% completeness level (i.e., every source in the region has a 50% or higher chance of not being recovered by our photometry). Unless otherwise specified, from this point onward we will refer only to stars above the 50% completeness limit in their respective tiles. To fit the colors of the very young stars in the RSG sequences, we assumed two different metallicity values for the two galaxies: $[\text{Fe}/\text{H}] = -0.6$ for NGC 4485 (i.e., tiles 1 and 5); and $[\text{Fe}/\text{H}] = -0.3$ for the rest of the tiles belonging to NGC 4490 (see Section 3.3 for a more in-depth discussion). On the other hand, an old population of stars with $[\text{Fe}/\text{H}] = -1.2$ seems to well fit the color of the RGB branch of both NGC 4485 and NGC 4490.

The CMDs of tiles 1 and 5 show an extremely tight and well-populated RSG sequence at $m_{\text{F115W}} - m_{\text{F200W}} \sim 1$ mag, covering a magnitude range from $m_{\text{F200W}} \sim 18$ mag to ~ 24 mag. In tile 5 (i.e., in the bridge), the RSG sequence displays a clear gap in the magnitude interval $24 \text{ mag} \lesssim m_{\text{F200W}} \lesssim 22 \text{ mag}$ (see also Figure 5). The most likely explanation for such a paucity of stars in this region of the CMD is that the galaxy experienced a period of low star formation activity between ~ 50 and 200 Myr ago (as indicated by the isochrones’ ages), followed by a strong burst that began around 30 Myr ago and lasted until very recent epochs (~ 5 Myr ago). Another very interesting feature, present in tile 1 (i.e., in the main body of NGC 4485) is a second red “finger,” above the tip of the RGB, running almost parallel to

the RSG sequence (also marked in Figure 5). This sequence is mostly populated by relatively massive O-rich AGB stars with ages that span between ~ 100 and ~ 200 Myr. Less evolved He-burning stars of the same age form also a striking overdensity cloud around $m_{\text{F115W}} - m_{\text{F200W}} \sim 0.5$ mag and $m_{\text{F200W}} \sim 25$ mag (already highlighted in Figure 5). The definitive proof that these stars trace the same population is given by the fact that in tile 5, where we do not observe a prevalent O-rich AGB finger, the fainter BL overdensity is also absent. The tight magnitude range covered by the He-burning star overdensity allows us to infer the birth epoch of this population with great precision to around 100 – 200 Myr ago (see isochrones in tile 1 panel of Figure 5). Moreover, the lower number of stars brighter or fainter than this feature points to the bursty nature of this star formation event. Interestingly, the age of this burst seems to agree remarkably well with the time of the second close encounter between the two galaxies, independently predicted by S. Pearson et al. (2018)’s *N*-body simulations. In the CMDs of both tiles we recovered a red and bright ($m_{\text{F200W}} \sim 22$ mag) horizontal “tail,” with a large color range, from ~ 1.5 to ~ 4 mag, populated by C-rich AGB stars with ages between ~ 200 Myr and ~ 1 Gyr. Finally, the most populated feature in both CMDs is the RGB, composed of very old (age $\gtrsim 1$ Gyr), low-mass stars that trace the earlier (possibly the earliest) epochs in the life of the galaxy.

The CMD of tile 9 in Figure 6, covering NGC 4490’s side of the bridge region, displays many similarities with that of tile 5, including a similar paucity of stars in the RSG sequence around $m_{\text{F200W}} \sim 22.5$ mag, pointing to a synchronized onset of this starburst event. Interestingly, tile 10’s CMD seems to display a young population with similar characteristics to those observed in the bridge (tile 9), an RSG sequence with a clear break, and the absence of an O-rich AGB finger, even though tile 10 covers a bright star-forming region to the northeast of

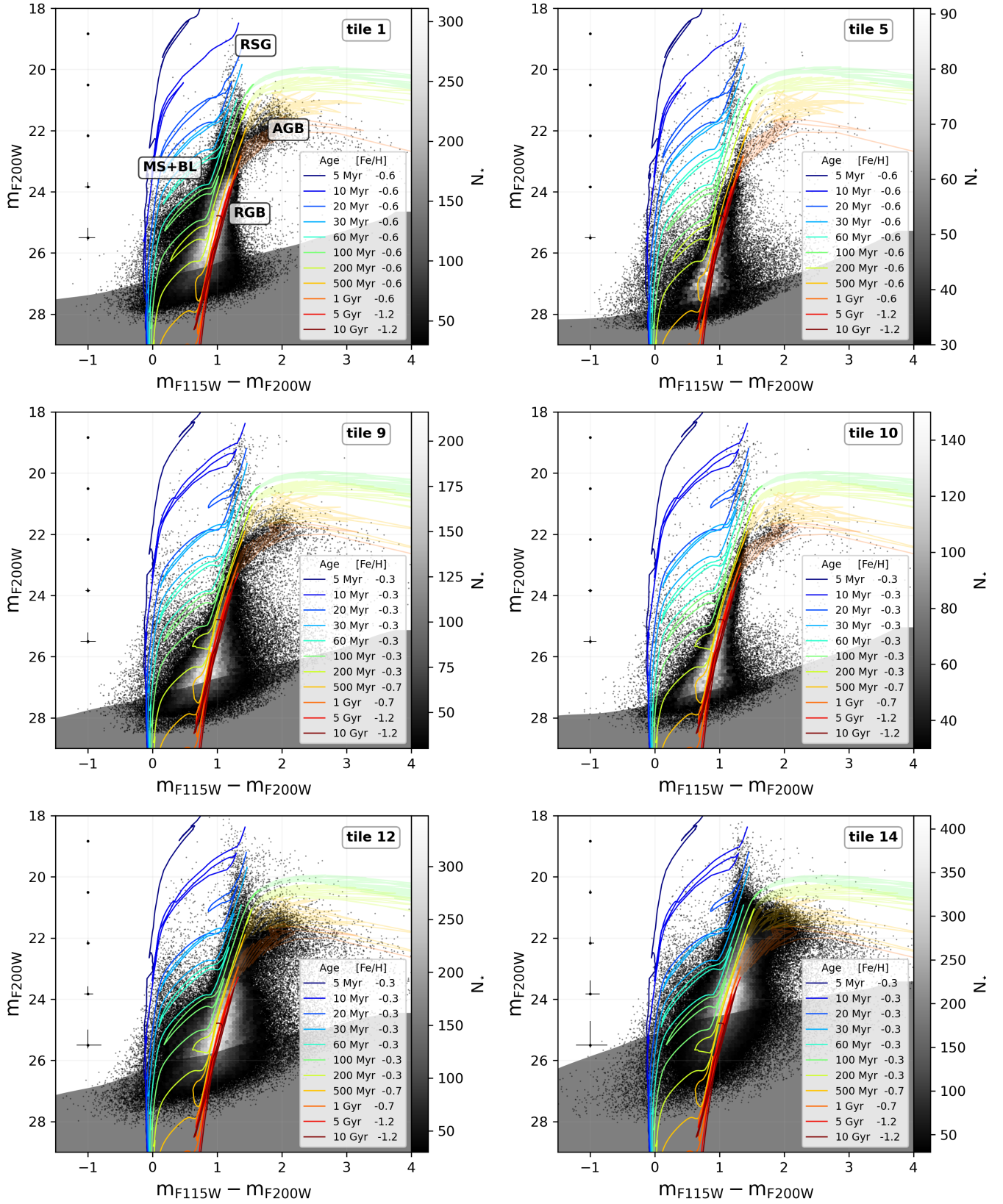


Figure 6. CMDs of tiles 1, 5, 9, 10, 12, and 14 covering different regions of both NGC 4485 and NGC 4490. Each CMD is binned and color coded according to the density of stars. Different sets of PARSEC-COLIBRI isochrones are also plotted, assuming a distance modulus of $(m - M)_0 = 29.70$ and a reddening of $E(B - V) = 0.15$, color coded according to age and metallicity (see legend on the bottom right of each panel). The TPAGB phase is shown with a lower α value. Photometric errors estimated from ASTs are shown on the left-hand side. The shaded area marks the 50% completeness limit. Some of the stellar evolutionary phases mentioned in the text are labeled in the tile 1 CMD.

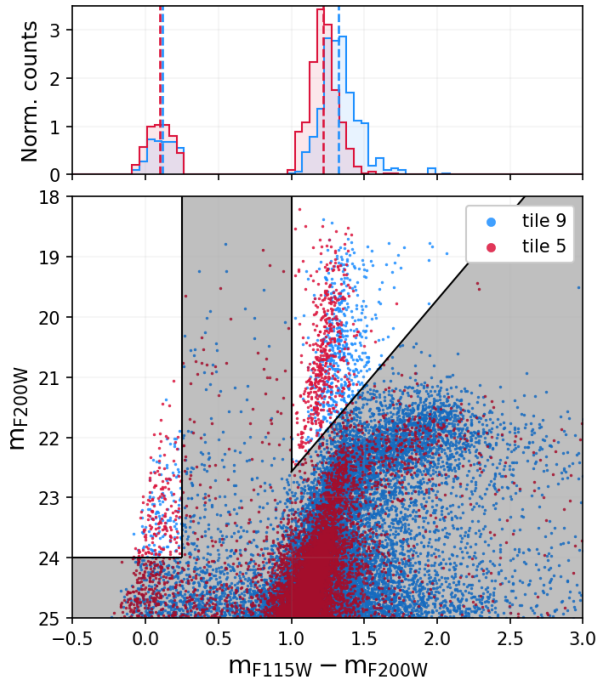


Figure 7. Bottom panel: comparison between the CMDs of tile 5 (red points) and tile 9 (blue points). Top panel: normalized distributions as a function of color of the upper MS and RSG sequences for tiles 5 and 9, after exclusion of the shaded area to avoid contamination from other stellar evolutionary phases and photometric errors. The dashed vertical lines represent the median colors of the tile 5 and tile 9 upper MS and RSG sequences.

the bridge. The projected distance between these two star-forming regions (~ 2 kpc) limits the possible explanations for this tightly synchronized burst to gravitational interaction with NGC 4485. Finally, tiles 12 (covering a bright star-forming region next to the NGC 4490 part of the bridge) and 14 (which covers the optical center of NGC 4490; A. Lawrence et al. 2020) show all of the main features discussed above. These include a very bright RSG sequence without any breaks, a well-populated BL sequence corresponding to isochrones with ages between approximately 100 and 200 Myr, and bright O-rich and C-rich AGB stars. A pronounced RGB sequence is also present. The CMDs of both tiles, which cover intrinsically crowded regions of the galaxy, are affected by shallower and more uncertain photometry due to the more intense crowding conditions. Readers interested in a detailed analysis of the remaining tiles’ CMDs are referred to the [Appendix](#).

3.3. Metallicity Gradient

Aside from different stellar chemical compositions, we also explored other potential explanations for the substantial shift in color of the young RSG sequence stars across the bridge (see Section 3.2), such as photometric errors or internal reddening. The former mechanism can be rejected, since it would cause only a higher spread around the mean color of the RSG sequence rather than a systematic shift in color, while the latter would cause also a corresponding shift in the blue edge of the upper MS stars, which we do not observe. For instance, Figure 7 shows a comparison between the CMDs of tiles 5 and 9 (see bottom panel), focusing in particular on the difference in the average color between the two RSG sequences and the blue edge of the upper MS. We observe a clear shift of ~ 0.2 mag in

the median color of the two RSG sequences (vertical dashed red and blue line, respectively), without seeing a corresponding shift in the color of the upper MS (see top panel of Figure 7). This finding confirms the presence of a significant chemical composition gradient among the young stellar populations of the bridge between the two dwarf galaxies. Recently, S. Duarte Puertas et al. (2025, in preparation) mapped the system’s gas-phase oxygen abundance as part of the SIGNALS survey (L. Rousseau-Nepton et al. 2019) with the imaging Fourier transform spectrograph SITELE (L. Drissen et al. 2019). Interestingly, the authors found that the gas in NGC 4485 is substantially more metal poor than that in NGC 4490, with a clear gradient across the tidal bridge connecting the two galaxies, consistent with what we find in the young stellar component. Moreover they found a pocket of metal-poor gas corresponding to the star-forming complex on the northeast side of NGC 4490 (located in tiles 10 and 13).

Taken together, our results and those of S. Duarte Puertas et al. (2025, in preparation) point to a scenario in which the most recent pericenter passage (which occurred ~ 200 Myr ago) stripped metal-poor gas from NGC 4485, likely due to a combination of tidal interactions and ram pressure (L. Mayer et al. 2006). Subsequently, this gas appears to have partially mixed with the more metal-rich gas of NGC 4490, fueling simultaneously the very recent burst ($\lesssim 30$ Myr) of star formation in the bridge (i.e., tiles 5 and 9) and in the northwest side of NGC 4490 (i.e., tile 10).

3.4. The Spatial Distribution of Stars

To investigate the interaction history between NGC 4485 and NGC 4490, we isolate and select different regions in the CMD of both dwarf galaxies (see Section 3.1), tracing different stellar phases and age ranges, to study their spatial distribution across our field of view. In particular, we identify three distinct CMD regions, with color and magnitude limits guided by careful comparisons between the CMDs and PARSEC-COLIBRI stellar isochrones (see Figure 6). Figure 8 illustrates our selections of stars for NGC 4485’s CMD, which includes tiles 1, 2, 3, 4, and 5. Similar methodologies and selections have been applied to NGC 4490’s CMD including the remaining tiles.

The shaded area in blue highlights young MS stars, RSGs, as well as more evolved BL stars, and O-rich AGB stars. The strict magnitude limit at $m_{F200W} = 26$ mag is imposed to minimize the influence of photometric errors leading to population mixing and incompleteness effects in our analysis. Additionally, we exclude redder stars to avoid contamination from older AGB and RGB stars. This selection corresponds to an age range $\lesssim 200$ Myr. Stars in the bright horizontal red “tail,” shaded in green, are mostly C-rich AGB stars, tracing intermediate epochs, spanning from ~ 200 Myr to ~ 1 Gyr. We note that, due to the known uncertainties affecting carbon-rich AGB models (P. Ventura et al. 2018), the age limits associated with this selection are somewhat uncertain. Finally, the region shaded in red at $m_{F115W} - m_{F200W} \sim 1.25$ mag and $23.8 \text{ mag} \lesssim m_{F200W} \lesssim 26 \text{ mag}$ is dominated by low-mass RGB stars older than ~ 1 Gyr, and potentially as old as ~ 13 Gyr. Again, the $m_{F200W} < 26$ mag limit is imposed to mitigate undesired effects due to large photometric errors affecting fainter stars and severe incompleteness that might weaken our conclusions.

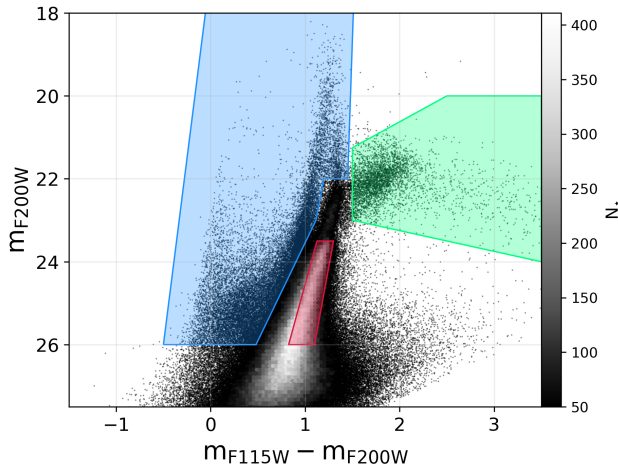


Figure 8. CMD of NGC 4485 (i.e., tiles 1, 2, 3, 4, and 5) showing our selection of three different stellar populations, tracing different epochs in the life of the galaxy. MS, BL, RSG, and O-rich AGB stars younger than 200 Myr are in blue. C-rich AGB stars between ~ 200 Myr and ~ 1 Gyr are in green, and RGB stars older than ~ 1 Gyr, and potentially as old as ~ 13 Gyr, are in red.

In addition, we further divide our youngest stellar population selection (the one in blue in Figure 8) into four smaller age bins: younger than 25 Myr, from 25 to 50 Myr, from 50 to 100 Myr, and from 100 to 200 Myr. The choice of this particular age binning size is driven by the need to have enough time sensitivity to best study the most recent star formation history, but without compromising our results due to small number statistics or inherent population mixing due to uncertainties from photometric errors. To accomplish this we follow a procedure similar to what is described in M. Correnti et al. (2025b). We first generated two well-populated synthetic CMDs, assuming PARSEC-COLIBRI stellar models, a P. Kroupa (2001) initial mass function, a constant SFR in the last 800 Myr, a distance modulus of $(m - M)_0 = 29.70$, a reddening of $E(B - V) = 0.15$, and $[\text{Fe}/\text{H}] = -0.6$ and $[\text{Fe}/\text{H}] = -0.3$ for NGC 4485 and NGC 4490, respectively. Then, after convolving the “clean” synthetic CMDs with the photometric errors and completeness characteristic of each galaxy, we are ready to associate an age to each observed source. For each observed star, we selected all synthetic stars whose positions in the CMD lie within a radius of 0.1 mag and computed the mean and standard deviation of their age distribution, which are then assigned to the observed star. If fewer than five synthetic stars are found within this radius, we progressively increase the radius in steps of 0.05 mag until a minimum of five stars is reached. Finally, each observed star is assigned to its respective age bin.

Figures 9 and 10 show the spatial distributions of the stars belonging to the different age selections described above, overlaid on the F200W NIRC2 image. In the left panels we show the total CMDs of NGC 4485 and NGC 4490 in gray, with the selected stars belonging to that particular age interval in red. To help the reader, we also plot three isochrones (black dashed lines), with ages of 10 Myr, 100 Myr, and 1 Gyr, respectively. In the right panel, we binned the distribution of stars and plot a 2D histogram color coded according to the number of stars that fall in each cell (going from dark red to white, see the color bar on the right-hand side). In the upper-left corner we reported the total number of selected stars in each galaxy. The blue cross and star symbols mark the

locations of the optical and dust-shrouded IR nuclei of NGC 4490 found by A. Lawrence et al. (2020), respectively.

Looking in more detail at the spatial distribution of our selected bona fide stars younger than 25 Myr (upper panel of Figure 9), we observe a distinct tidal tail extending from NGC 4485. This tail is connected to NGC 4485’s center and is oriented toward NGC 4490 in the southwest direction, where it terminates in two compact and highly active star-forming regions at $x \sim 2000$ and $y \sim 2000$. In contrast, the young stellar population in NGC 4490 exhibits a more complex morphology. We identify a star-forming disk extending from the northwest to the southeast, as well as more prominent clumps of young stars in the spiral arms, particularly on the disk’s northeast side at $x \sim 7000$ and $y \sim 1000$. At $x \sim 5000$ and $y \sim 4000$, a star-forming complex extends toward NGC 4485 and completes the bridge structure.

Moving to the next age bin, i.e., $25 \text{ Myr} \lesssim \text{age} \lesssim 50 \text{ Myr}$ (middle panel of Figure 9), we can still distinguish a well-populated final section of NGC 4485’s tidal tail, but complemented by a relative higher number of stars present in the main body of the dwarf galaxy. For NGC 4490, we observe a strong overdensity in the position of the optical nucleus (marked by the blue cross; A. Lawrence et al. 2020), and a pronounced tail on the east side of the disk at $x \sim 9000$ and $y \sim 500$. Stars in the age interval between 50 and 100 Myr (lower panel of Figure 9) in NGC 4485 show a more concentrated distribution around the center of the galaxy, with an even lower ratio between the number of stars forming the bridge versus the core. In NGC 4490, these stars are distributed in a similar fashion compared to the previous age bin, except for the appearance of what seems like a second high-density peak positioned to the east of the optical nucleus, around $x \sim 8500$ and $y \sim 1500$.

The top panel of Figure 10 shows the spatial distribution of our selected stars from 100 to 200 Myr. These stars trace the time frame in which S. Pearson et al. (2018) predicted the latest close pericenter passage between the two dwarfs to happen. NGC 4485 displays a high concentration of stars in its core with respect to the star-forming regions in the bridge. This finding seems to confirm that a strong starburst occurred in the center of NGC 4485, probably triggered by the compression of the gas due to the interaction with NGC 4490 (B. G. Elmegreen 1998). This passage is also likely responsible for the stripping of the H I gas that later collapsed to form the bright H II regions in the bridge. On the other hand, NGC 4490 shows all the features already present in the previous age intervals, with no particular overdensities in both nuclei. We warn the reader that this lack of peaks in the center of NGC 4490 might be due to the intrinsic lower completeness in this region. Nevertheless, NGC 4490’s disk, spiral arms, and tidal tails are still visible, suggesting that the interaction with the companion has triggered spatially diffuse star formation episodes across the galaxy.

The middle panel of Figure 9 shows the spatial distribution of our selection of intermediate-age ($200 \text{ Myr} \lesssim \text{age} \lesssim 1 \text{ Gyr}$) C-rich AGB stars, forming the horizontal red “tail” in the CMDs. As expected, their distribution in both dwarf galaxies looks less clumped compared to younger stars, and more uniform across the bodies of the two dwarf galaxies. Interestingly, we report that NGC 4490 seems to show a peak of stars close to the location of the IR nucleus reported by A. Lawrence et al. (2020). Moreover, in the region between the two dwarfs, we recovered some stars bridging between the two halos.

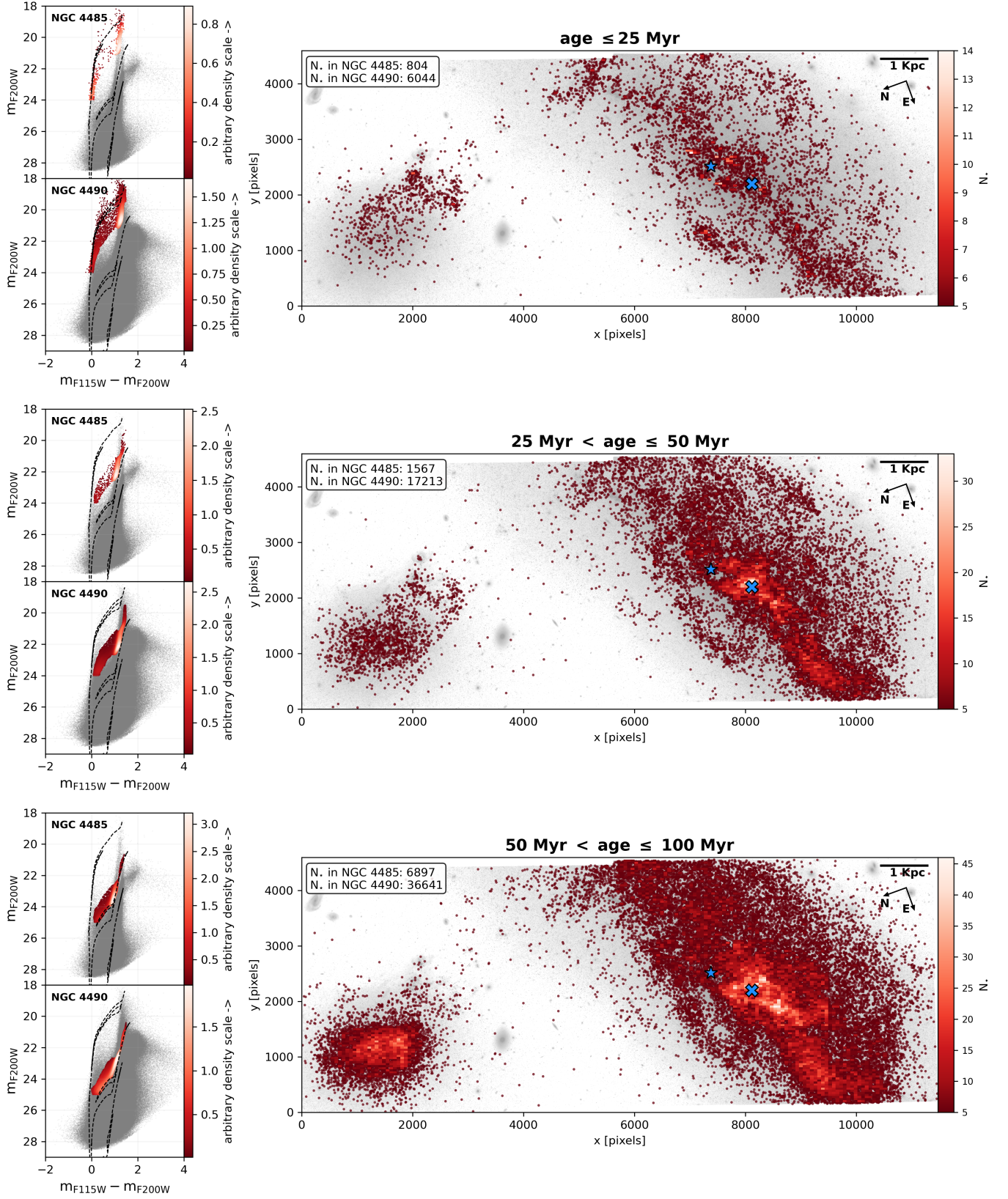


Figure 9. CMDs and spatial distributions of NGC 4485 and NGC 4490 stars in different age intervals: age ≤ 25 Myr, 25 Myr < age ≤ 50 Myr, and 50 Myr < age ≤ 100 Myr. Left panels: NGC 4485 (upper panel) and NGC 4490 (lower panel) CMDs, with the stars in the selected age intervals marked in red, and with the PARSEC-COLIBRI 10 Myr, 100 Myr, and 1 Gyr isochrones in dashed black lines. Right panels: spatial distributions of the stars in the selected age intervals, overlaid on the F200W reference image. In the high-density regions, the data are binned and color coded according to the number of points (see the color bar on the right-hand side of each panel). The cross and star symbols mark the positions of the optical and IR nuclei, respectively, as reported by A. Lawrence et al. (2020). The number of stars in the selected age interval for both NGC 4485 and NGC 4490 is reported in the upper left.

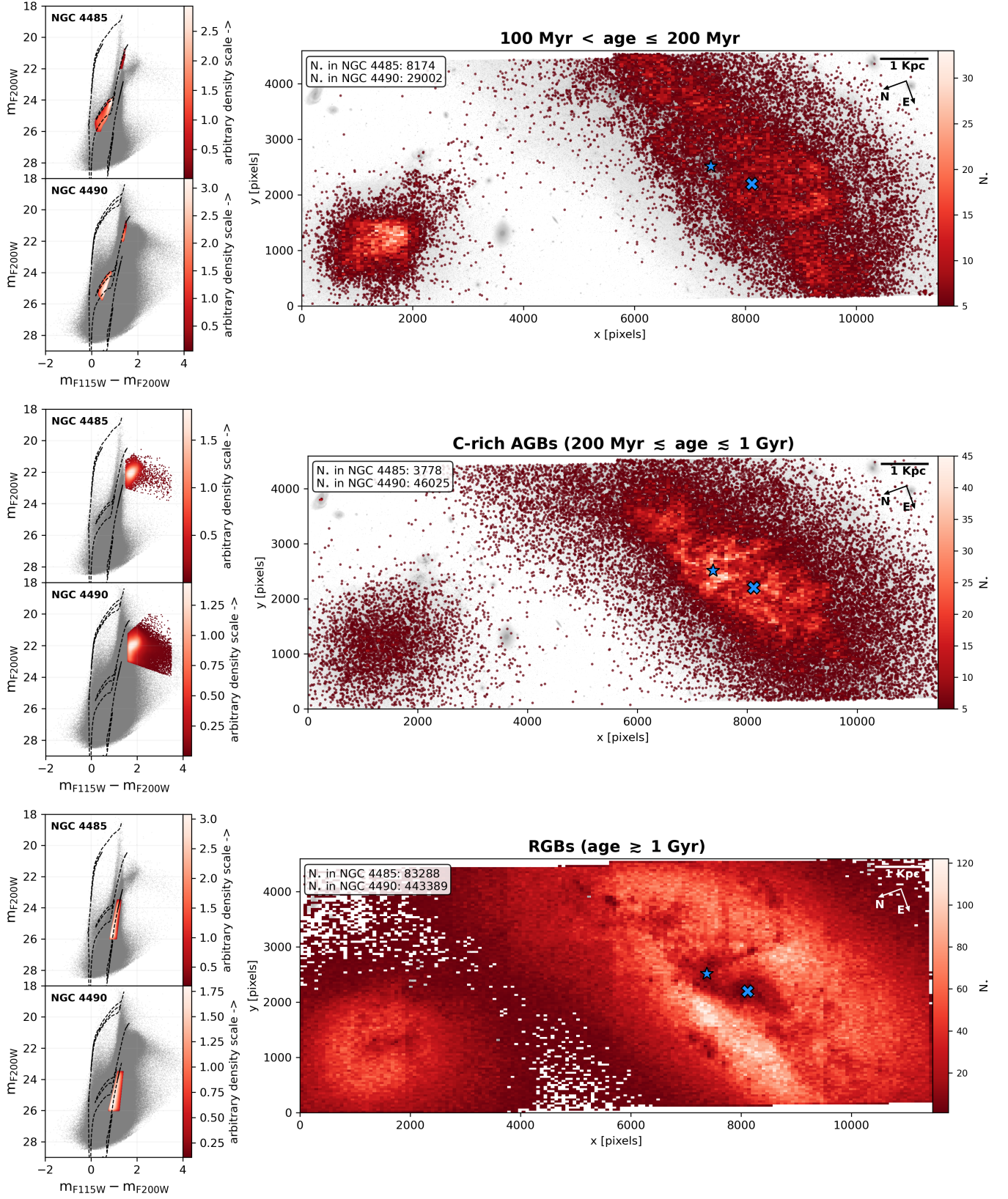


Figure 10. Same as Figure 9, but for selected bona fide stars with ages between ~ 100 and ~ 200 Myr, intermediate-age C-rich AGB stars between 200 Myr and 1 Gyr, and RGB stars older than 1 Gyr.

The bottom panel of Figure 10 shows the spatial distribution of a sample of old ($\text{age} \gtrsim 1$ Gyr) RGB stars. The intrinsic faintness of these stars makes them prone to suffer from

completeness issues at this distance. For this reason, we restricted our samples for both galaxies from $m_{F200W} = 23.8$ mag (the location of the tip) to

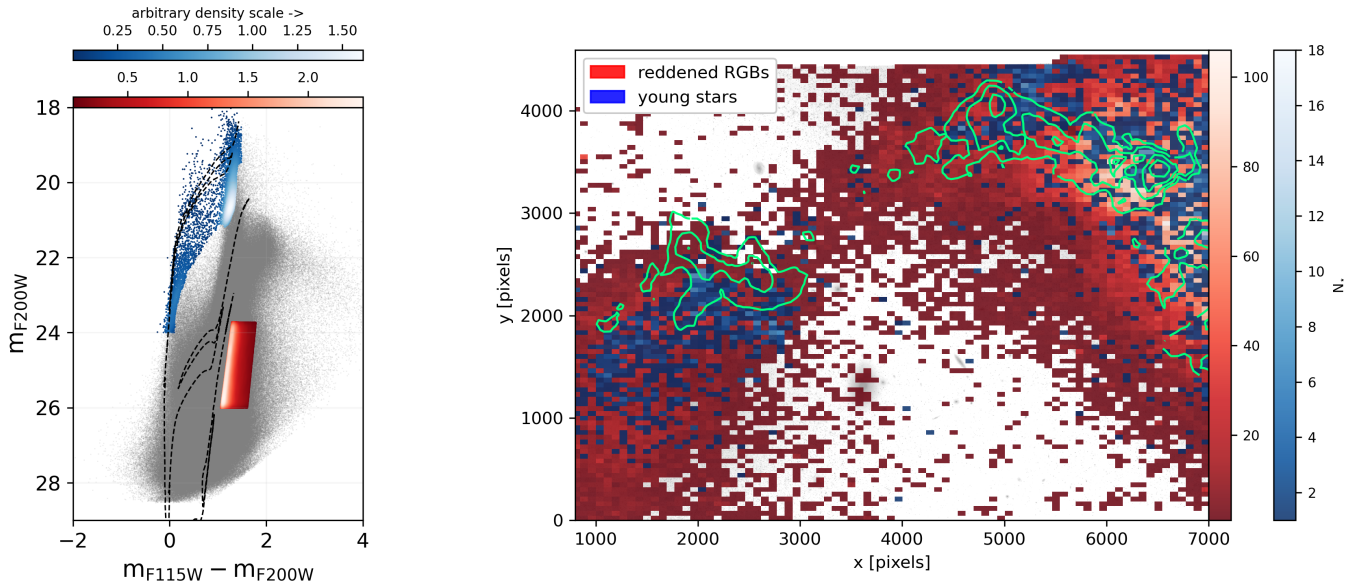


Figure 11. Left panel: CMD of the entire NIRCam field of view, with the selected populations of young stars (in blue) and reddened RGBs (in red). Right panel: comparison between the spatial distribution in the bridge region of reddened RGB stars (in red), and our selection of bona fide young stars (age ≤ 25 Myr, see top panel of Figure 9) in blue. The data are color coded according to their number density (see the color bars on the right-hand side). H I contours in green at $[4, 6, 8, 10] \times 10^{21} \text{ cm}^{-2}$ from a VLA B-configuration ($7''$ beam) pilot program (Cannon et al. 2025, private communication) are also shown.

$m_{F200W} = 26$ mag. Despite this precaution, most “holes” in the spatial distribution of this sample, especially closer to the centers of the galaxies and bright star-forming regions, are most likely due to a combination of incompleteness and possibly extinction from dust lanes (see the red channel in Figure 2). The long lives of these stars make them subject to the effects of orbital mixing (R. A. Ibata et al. 1997; A. Helmi & S. D. M. White 1999; A. P. Cooper et al. 2010; V. Belokurov et al. 2018), thus they show a broad and uniform distribution, occupying most of the field of view. We report, somewhat surprisingly, that the old stellar halos of the two dwarf galaxies seem not to have been strongly perturbed despite the close gravitational interaction between the two bodies (see, e.g., R. Pascale et al. 2024; E. Sacchi et al. 2024). Nevertheless, this is most likely due to our restricted field of view (see Figure 1), since faint and extended tidal features have been observed in deep ground-based imaging (see, e.g., D. M. Elmegreen et al. 1998; B. J. Smith et al. 2010; S. Pearson et al. 2018; A. Lawrence et al. 2020; S. Mandal & C. R. Kerton 2024).

Finally, in Figure 11, we compare the spatial distribution of a selection of RGB stars that are redder than the average color predicted by stellar models, along with our previous selection of RGB stars (see left panel), to our sample of stars younger than 25 Myr (see top panel of Figure 9). We focus in particular on the bridge region, where the RGB stars appear to outline a fully connected bridge between the two dwarf galaxies, around $x \sim 4000$ and $y \sim 3000$, aligned with the positions of the youngest stars (shown in blue) and H I contours from a VLA B-configuration pilot program (Cannon et al. 2025, private communication). These RGB stars are likely redder due to the presence of dust mixed with the gas. Therefore, this population can be used to trace regions of higher gas density and extinction. This result reinforces the idea that a gas/dust lane connects the two dwarf galaxies, likely created during their most recent close encounter through tidal and ram pressure stripping, and currently

sustaining the ongoing star formation observed in these regions (S. Mandal & C. R. Kerton 2024).

4. Summary and Conclusions

In this paper, we presented new JWST/NIRCam observations of the closest known interacting dwarf galaxy pair, NGC 4485–NGC 4490, obtained as part of the Cycle 1 FEAST program (A. Adamo et al. 2025, in preparation). This system offers a unique laboratory for studying galaxy interactions at the smallest scales, providing valuable insights into how such processes may shape galaxy formation and evolution at high redshift. Our main goal was to probe, for the first time, the resolved stellar populations of this remarkable system in the NIR, leveraging JWST’s exquisite capabilities. Here we summarize our main findings.

1. The NIRCam data (see Figure 2) confirm the presence of a young stellar bridge connecting the two dwarf galaxies, composed of bright H II regions that trace a dense gas bridge fueling the active star formation. This bridge is likely the result of tidal and/or ram pressure stripping that has occurred during the last close encounter between the two companions (M. S. Clemens et al. 2000; S. Pearson et al. 2018; S. Mandal & C. R. Kerton 2024).
2. The NIR CMDs of the galaxies host an impressive variety of stellar populations from tile to tile, spanning a substantial range in age and metallicity. Both galaxies show prominent populations of young ($\lesssim 200$ Myr) upper MS, BL, and O-rich AGB stars. In particular, we report the presence of well-populated RSG branches reaching in some cases up to $m_{F200W} \sim 18$ mag. We also detect a substantial population of intermediate-age C-rich AGB stars, occupying a well-defined red “tail” in the CMDs. We recover a robust RGB sequence populated by low-mass stars, older than 1 Gyr.

3. Tiles 5 and 9 (which cover the bridge region), along with tile 10 (a star-forming region on the northeastern side of NGC 4490), show a clear gap in their RSG sequences at $m_{F200W} \sim 23$, followed by a prominently populated brighter section. This morphology can only be explained by an intense burst of star formation between ~ 5 and 30 Myr ago. Moreover, we found a significant difference in the average color (~ 0.2 mag) of the RSG sequences of tiles 5 and 9. This difference in color translates to a factor of 2 difference in the metal content of the respective young stellar populations (assuming a solar abundance pattern). This result strongly supports the scenario in which metal-poor gas stripped from NGC 4485 was mixed with the more metal-rich gas of NGC 4490, before forming the young population of stars we observe in the bridge region and around the main body of NGC 4490.
4. In NGC 4485, we identify an overdensity of blue He-burning stars around $m_{F115W} - m_{F200W} \sim 0.5$ mag and $m_{F200W} \sim 25$ mag. The properties of this stellar evolutionary phase allow us to precisely date the associated burst of star formation to approximately 100–200 Myr ago. Our findings are in very good agreement with the independent predictions by S. Pearson et al. (2018), based on N -body simulations, which place the system’s last pericenter passage at around 230 Myr ago.
5. We compared the spatial distributions of a sample of bona fide stellar populations, selected from the observed CMDs using synthetic CMDs generated from PARSEC–COLIBRI stellar models, tracing different epochs spanning the entire history of the system. The spatial distribution of the youngest stars (≤ 25 Myr) shows a tidal tail extending from the center of NGC 4485 connecting to NGC 4490’s disk through the bridge. NGC 4490 also shows compact star-forming regions associated with its spiral arms that originate from the IR nucleus. The population tracing the age range 100–200 Myr shows a significant overdensity of stars in the core of NGC 4485 with respect to the bridge region. This result supports the hypothesis of an intense central starburst in NGC 4485, likely initiated by gas compression resulting from its recent close interaction with NGC 4490. Finally, the stellar populations tracing older epochs (i.e., AGB and RGB stars) show a more uniform distribution, with no particular evidence of perturbation.
6. The spatial distribution of a selection of reddened RGB stars closely traces the location of the young star-forming regions identifying a continuous bridge connecting the two interacting galaxies (see Figure 11). These stars appear redder due to the presence of dust within the H I gas. This result suggests the presence of a dense gas/dust lane connecting the two dwarf galaxies, as confirmed by independent VLA B-configuration observations (Cannon et al. 2025, private communication).

The study of the resolved stellar populations presented in this paper, combined with previous N -body simulations (S. Pearson et al. 2018) and upcoming investigations of the ISM properties (S. Duarte Puertas et al. 2025, in preparation), adds upon and improves our picture of the interaction history of the NGC 4485–NGC 4490 dwarf galaxy system. This work represents a first step toward a more detailed analysis of our JWST data, which will include deriving the system’s spatially

resolved star formation history through CMD modeling (G. Bortolini et al. 2025, in preparation). Our results, together with other recent studies of resolved stellar populations in Local Volume galaxies (see, among others, D. R. Weisz et al. 2023; G. Bortolini et al. 2024b; N. Habel et al. 2024; K. B. W. McQuinn et al. 2024; C. Nally et al. 2024; M. Correnti et al. 2025b), demonstrate the remarkable capabilities of JWST, far exceeding those of previous IR telescopes and providing unprecedented insights into the star formation processes of nearby dwarf galaxies.

Acknowledgments

The authors wish to thank the anonymous reviewer for their insightful comments, which helped improve the manuscript. A.A. acknowledges support from Vetenskapsrådet 2021-05559. A.A. and A.P. acknowledge support from the Swedish National Space Agency (SNSA) through the grant 2021-00108. A.A. and H.F.V. acknowledge support from (SNSA) 2023-00260. K.G. is supported by the Australian Research Council through the Discovery Early Career Researcher Award (DECRA) Fellowship (project number DE220100766) funded by the Australian Government. K.G. is supported by the Australian Research Council Centre of Excellence for All Sky Astrophysics in 3 Dimensions (ASTRO 3D), through project number CE170100013. This work is based in part on observations made with the NASA/ESA/CSA James Webb Space Telescope, which is operated by the Association of Universities for Research in Astronomy, Inc., under NASA contract NAS 5-03127. These observations are associated with program #1783. Support for program #1783 was provided by NASA through a grant from the Space Telescope Science Institute, which is operated by the Association of Universities for Research in Astronomy, Inc., under NASA contract NAS 5-03127. M.M. acknowledges financial support through grants PRIN-MIUR 2020SKSTHZ, the INAF GO Grant 2022 “The revolution is around the corner: JWST will probe globular cluster precursors and Population III stellar clusters at cosmic dawn,” and by the European Union—NextGenerationEU within PRIN 2022 project n.20229YBSAN —“Globular clusters in cosmological simulations and lensed fields: from their birth to the present epoch.

Data Availability

The data supporting the findings of this study are openly available at the following MAST doi:[10.17909/ybh0-r149](https://doi.org/10.17909/ybh0-r149). The full FEAST data releases can be downloaded from <https://feast-survey.github.io/>.

Facility: JWST (NIRCam).

Software: DOLPHOT (<http://americano.dolphinsim.com/dolphot/>; A. E. Dolphin 2000; A. Dolphin 2016), Astropy (Astropy Collaboration et al. 2013, 2018, 2022), Numpy (C. R. Harris et al. 2020), Pandas (W. McKinney 2010), Scipy (P. Virtanen et al. 2020), Matplotlib (J. D. Hunter 2007), SAOImageDS9 (developed by the Smithsonian Astrophysical Observatory 2000, W. A. Joye & E. Mandel 2003), TOPCAT (M. B. Taylor 2005).

Appendix

Analysis of the Color–Magnitude Diagrams for the Remaining Tiles

Figures 12 and 13 show the CMDs for the remaining tiles not shown in the main text. PARSEC–COLIBRI stellar

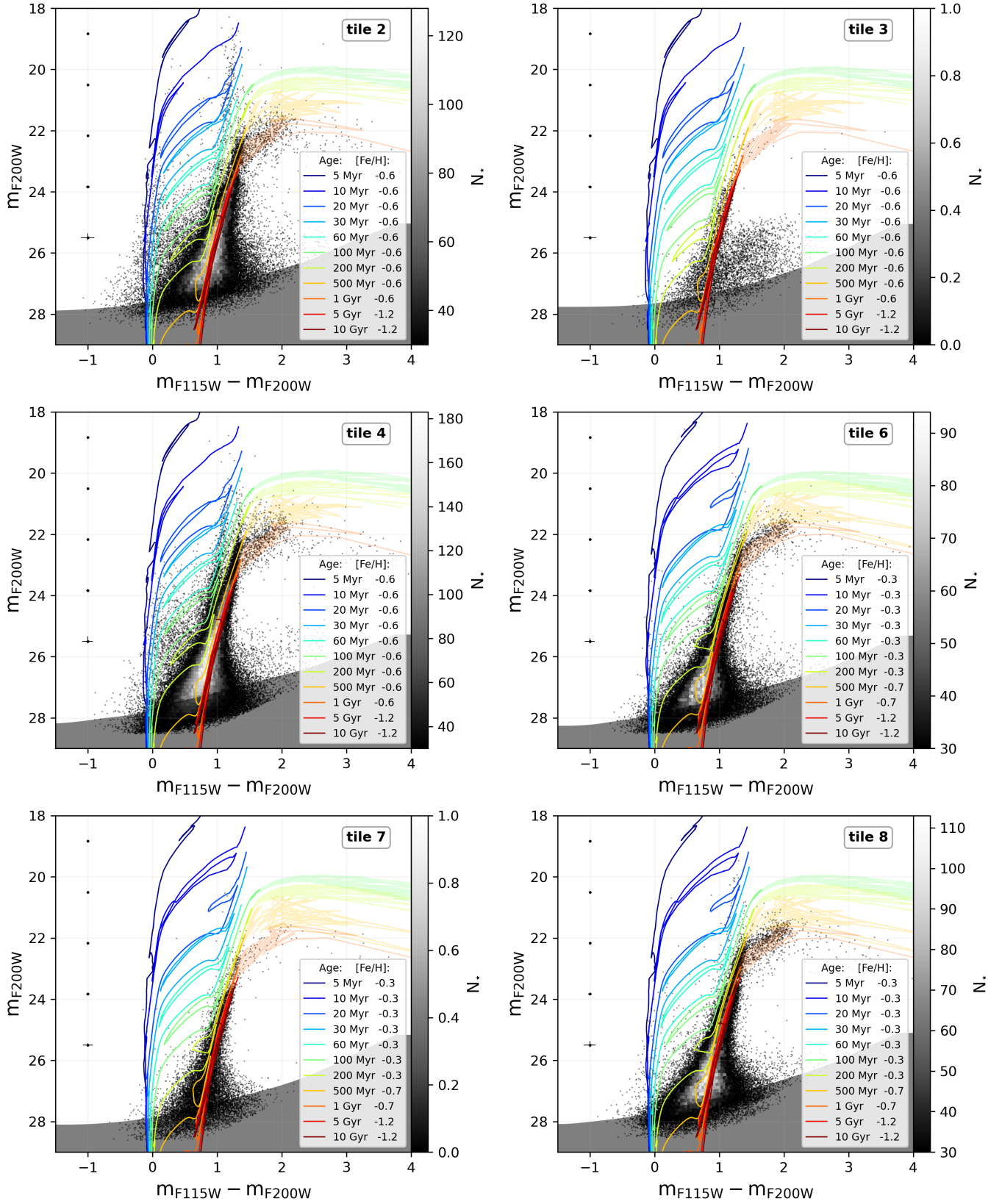


Figure 12. CMDs of tiles 2, 3, 4, 6, 7, and 8. See Figure 6.

isochrones are overplotted and color coded by their age and metallicity as in Figure 6. Photometric errors as a function of magnitude (error bars on the left-hand side) and the 50%

completeness limits (dark shaded area) are also reported. Tile 2, which covers part of the main body of NGC 4485, displays many similarities with tile 5, including a prominent population

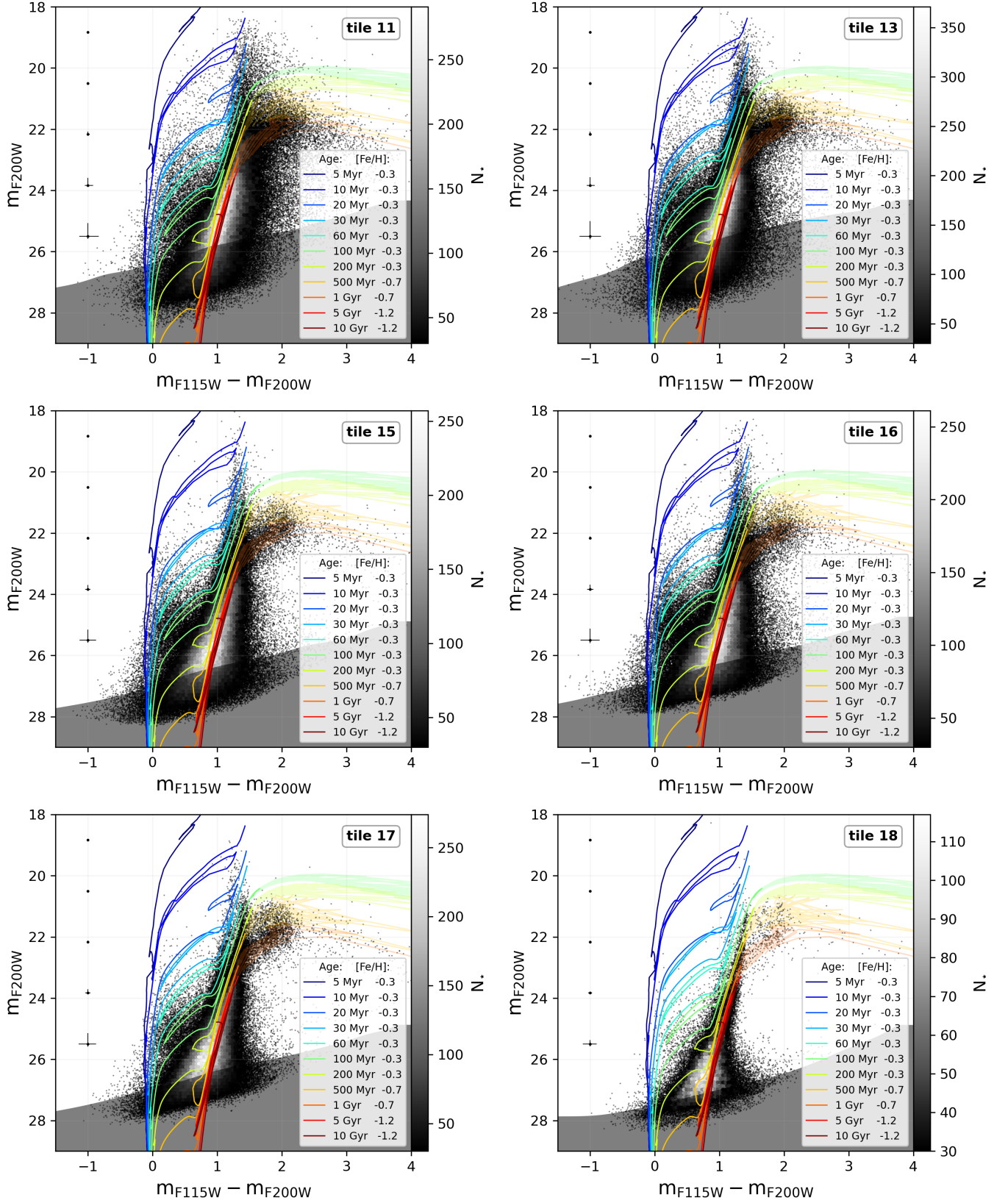


Figure 13. CMDs of tiles 11, 13, 15, 16, 17, and 18. See Figure 6.























of bright RSG stars, with a gap around $m_{F200W} \sim 23$ mag. Moreover, as in tile 5, it does not show any trace of the red O-rich AGB “finger” parallel to the RSG sequence, which is

instead clearly visible in the other tiles covering the main body of NGC 4485, namely tiles 1 and 4. Interestingly, tile 4 presents a well-defined RSG sequence, but without the gap

seen in tile 5. Tiles 3 and 7 are probably the simplest, displaying clear RGBs dominated by old ($\gtrsim 1$ Gyr) stars, with no signs of recent star formation. The very faint ($m_{F200W} \sim 26$ mag) and red ($m_{F115W} - m_{F200W} \sim 1.5$ mag) sources that can be seen in tile 3 consist mostly of background galaxies. Indeed, due to the intrinsic low number of stars detected in this tile, the sharpness and crowding sigma clipping that was applied to the other tiles is too restrictive. We chose not to modify the cuts since we do not encounter the same problem in more populated tiles and given that we did not use that particular region of the CMD in any of our analysis. Tiles 6 and 8 cover the outer portion of the tidal bridge between the two dwarf galaxies. Both diagrams show a prominent old RGB, topped by a well-populated red “tail” of C-rich AGB stars. In both diagrams, only sparse signs of recent star formation are visible, with a few stars found in the upper MS and BL phases.

Most of the central tiles of NGC 4490, i.e., tiles 11, 13, 15, 16, and 17, show the same main features discussed for NGC 4485’s CMDs (even if affected in some case by a shallower and more uncertain photometry due to the more intense crowding conditions). A very bright RSG sequence; a well-populated BL sequence corresponding to the isochrones of ages between ~ 100 and 200 Myr, complemented by an O-rich red “finger” to the right of the RSG sequence; a pronounced red horizontal tail of TPAGB stars; and a dominant old RGB are seen. As expected, tile 18, which covers part of the outskirts of NGC 4490, is predominantly populated by old RGB stars. However, it also exhibits a sparsely populated group of BL stars around $m_{F200W} \sim 25$ mag, resembling the 100–200 Myr populations observed in other tiles of NGC 4490 and in NGC 4485. This suggests that traces of a recent pericenter passage between the two galaxies are also impressed in the low surface brightness outskirts of the system.

ORCID iDs

Giacomo Bortolini  <https://orcid.org/0009-0003-6182-8928>
 Matteo Correnti  <https://orcid.org/0000-0001-6464-3257>
 Angela Adamo  <https://orcid.org/0000-0002-8192-8091>
 Michele Cignoni  <https://orcid.org/0000-0001-6291-6813>
 Elena Sacchi  <https://orcid.org/0000-0001-5618-0109>
 Monica Tosi  <https://orcid.org/0000-0002-0986-4759>
 Göran Östlin  <https://orcid.org/0000-0002-3005-1349>
 Anastasios Kapodistrias  <https://orcid.org/0009-0009-2729-5025>
 Arjan Bik  <https://orcid.org/0000-0001-8068-0891>
 Daniela Calzetti  <https://orcid.org/0000-0002-5189-8004>
 Ana Duarte-Cabral  <https://orcid.org/0000-0002-5259-4774>
 Flavia Dell’Agli  <https://orcid.org/0000-0003-2442-6981>
 John S. Gallagher  <https://orcid.org/0000-0001-8608-0408>
 Benjamin Gregg  <https://orcid.org/0000-0003-4910-8939>
 Kathryn Grasha  <https://orcid.org/0000-0002-3247-5321>
 Thomas S.-Y. Lai  <https://orcid.org/0000-0001-8490-6632>
 Drew Lapeer  <https://orcid.org/0009-0009-5509-4706>
 Sean T. Linden  <https://orcid.org/0000-0002-1000-6081>
 Matteo Messa  <https://orcid.org/0000-0003-1427-2456>
 Alex Pedrini  <https://orcid.org/0000-0002-8222-8986>
 Elena Sabbi  <https://orcid.org/0000-0003-2954-7643>
 Linda J. Smith  <https://orcid.org/0000-0002-0806-168X>
 Helena Faustino Vieira  <https://orcid.org/0000-0002-2199-0977>
 John M. Cannon  <https://orcid.org/0000-0002-1821-7019>

Salvador Duarte Puertas  <https://orcid.org/0000-0002-5542-1940>

Carmelle Robert  <https://orcid.org/0000-0003-2344-6593>

References

- Annibali, F., Nipoti, C., Ciotti, L., et al. 2016, *ApJL*, **826**, L27
 Annibali, F., Beccari, G., Bellazzini, M., et al. 2020, *MNRAS*, **491**, 5101
 Annibali, F., & Tosi, M. 2022, *NatAs*, **6**, 48
 Annibali, F., Pinna, E., Hunt, L. K., et al. 2023, *ApJL*, **942**, L23
 Astropy Collaboration, Robitaille, T. P., Tollerud, E. J., et al. 2013, *A&A*, **558**, A33
 Astropy Collaboration, Price-Whelan, A. M., Sipőcz, B. M., et al. 2018, *AJ*, **156**, 123
 Astropy Collaboration, Price-Whelan, A. M., Lim, P. L., et al. 2022, *ApJ*, **935**, 167
 Bekki, K., & Chiba, M. 2005, *MNRAS*, **356**, 680
 Bellazzini, M., Ferraro, F. R., Sollima, A., Pancino, E., & Origlia, L. 2004, *A&A*, **424**, 199
 Bellazzini, M., & Pascale, R. 2024, *A&A*, **691**, A42
 Belokurov, V., Zucker, D. B., Evans, N. W., et al. 2006, *ApJL*, **642**, L137
 Belokurov, V., Erkal, D., Deason, A. J., et al. 2017, *MNRAS*, **466**, 4711
 Belokurov, V., Erkal, D., Evans, N. W., Koposov, S. E., & Deason, A. J. 2018, *MNRAS*, **478**, 611
 Besla, G., Kallivayalil, N., Hernquist, L., et al. 2010, *ApJL*, **721**, L97
 Bortolini, G., Cignoni, M., Sacchi, E., et al. 2024a, *MNRAS*, **527**, 5339
 Bortolini, G., Östlin, G., Habel, N., et al. 2024b, *A&A*, **689**, A146
 Bressan, A., Marigo, P., Girardi, L., et al. 2012, *MNRAS*, **427**, 127
 Calzetti, D., Lee, J. C., Sabbi, E., et al. 2015, *AJ*, **149**, 51
 Carlin, J. L., Sand, D. J., Price, P., et al. 2016, *ApJL*, **828**, L5
 Chambers, K. C., Magnier, E. A., Metcalfe, N., et al. 2016, arXiv, arXiv:1612.05560
 Cignoni, M., Sabbi, E., van der Marel, R. P., et al. 2016, *ApJ*, **833**, 154
 Clemens, M. S., Alexander, P., & Green, D. A. 1998, *MNRAS*, **297**, 1015
 Clemens, M. S., Alexander, P., & Green, D. A. 1999, *MNRAS*, **307**, 481
 Clemens, M. S., Alexander, P., & Green, D. A. 2000, *MNRAS*, **312**, 236
 Cooper, A. P., Cole, S., Frenk, C. S., et al. 2010, *MNRAS*, **406**, 744
 Correnti, M., Annibali, F., Bellazzini, M., et al. 2025a, *ApJ*, **982**, 31
 Correnti, M., Bortolini, G., Dell’Agli, F., et al. 2025b, *ApJ*, **990**, 72
 Crnojević, D., Sand, D. J., Spekkens, K., et al. 2016, *ApJ*, **823**, 19
 Diemand, J., Kuhlen, M., Madau, P., et al. 2008, *Natur*, **454**, 735
 Dohm-Palmer, R. C., Skillman, E. D., Saha, A., et al. 1997, *AJ*, **114**, 2527
 Dolphin, A. E. 2000, *PASP*, **112**, 1383
 Dolphin, A., 2016 DOLPHOT: Stellar photometry, Astrophysics Source Code Library, ascl:1608.013
 Drissen, L., Martin, T., Rousseau-Nepton, L., et al. 2019, *MNRAS*, **485**, 3930
 Elmegreen, B. G. 1998, in ASP Conf. Ser. 148, Origins, ed. C. E. Woodward, J. M. Shull, & H. A. Thronson Jr. (San Francisco, CA: ASP), 150
 Elmegreen, D. M., Chromey, F. R., Knowles, B. D., & Wittenmyer, R. A. 1998, *AJ*, **115**, 1433
 Frenk, C. S., White, S. D. M., Davis, M., & Efstathiou, G. 1988, *ApJ*, **327**, 507
 Gaia Collaboration, Vallenari, A., Brown, A. G. A., et al. 2023, *A&A*, **674**, A1
 Gardiner, L. T., & Noguchi, M. 1996, *MNRAS*, **278**, 191
 Garner, R., Mihos, J. C., & Rosales-Ortega, F. F. 2025, *ApJ*, **982**, 143
 Guglielmo, M., Lewis, G. F., & Bland-Hawthorn, J. 2014, *MNRAS*, **444**, 1759
 Habel, N., Nally, C., Lenkić, L., et al. 2024, *ApJ*, **971**, 108
 Hancock, M., Smith, B. J., Struck, C., Giroux, M. L., & Hurlock, S. 2009, *AJ*, **137**, 4643
 Harris, C. R., Millman, K. J., van der Walt, S. J., et al. 2020, *Natur*, **585**, 357
 Helmi, A., & White, S. D. M. 1999, *MNRAS*, **307**, 495
 Higgs, C. R., McConnachie, A. W., Irwin, M., et al. 2016, *MNRAS*, **458**, 1678
 Hunter, J. D. 2007, *CSE*, **9**, 90
 Ibata, R. A., Wyse, R. F. G., Gilmore, G., Irwin, M. J., & Suntzeff, N. B. 1997, *AJ*, **113**, 634
 Ibata, R., Irwin, M., Lewis, G., Ferguson, A. M. N., & Tanvir, N. 2001, *Natur*, **412**, 49
 Izotov, Y. I., & Thuan, T. X. 2009, *ApJ*, **690**, 1797
 Joye, W. A., & Mandel, E. 2003, in ASP Conf. Ser. 295, Astronomical Data Analysis Software and Systems XII, ed. H. E. Payne, R. I. Jedrzejewski, & R. N. Hook (San Francisco, CA: ASP), 489
 Kallivayalil, N., Sales, L. V., Zivick, P., et al. 2018, *ApJ*, **867**, 19
 Karachentsev, I. D., Kaisina, E. I., & Makarov, D. I. 2018, *MNRAS*, **479**, 4136
 Karachentsev, I. D., & Kroupa, P. 2024, *MNRAS*, **528**, 2805
 Kravtsov, A. V., Gnedin, O. Y., & Klypin, A. A. 2004, *ApJ*, **609**, 482
 Kroupa, P. 2001, *MNRAS*, **322**, 231

- Lawrence, A., Kerton, C. R., Struck, C., & Smith, B. J. 2020, [ApJ](#), **891**, 11
- Lee, M. G., Freedman, W. L., & Madore, B. F. 1993, [ApJ](#), **417**, 553
- Liu, Y., Zhu, M., Yu, H., et al. 2023, [MNRAS](#), **523**, 3905
- Maeder, A., & Meynet, G. 2001, [A&A](#), **373**, 555
- Makarov, D., Makarova, L., Rizzi, L., et al. 2006, [AJ](#), **132**, 2729
- Mandal, S., & Kerton, C. R. 2024, [MNRAS](#), **529**, 953
- Marigo, P., Girardi, L., Bressan, A., et al. 2017, [ApJ](#), **835**, 77
- Martínez-Delgado, D., Gabany, R. J., Crawford, K., et al. 2010, [AJ](#), **140**, 962
- Mayer, L., Mastropietro, C., Wadsley, J., Stadel, J., & Moore, B. 2006, [MNRAS](#), **369**, 1021
- McConnachie, A. W., Irwin, M. J., Ibata, R. A., et al. 2009, [Natur](#), **461**, 66
- McKinney, W. 2010, in Proc. of the 9th Python in Science Conference, ed. S. van der Walt & J. Millman, 56
- McQuinn, K. B. W., B. Newman, M. J., Savino, A., et al. 2024, [ApJ](#), **961**, 16
- Nally, C., Jones, O. C., Lenkić, L., et al. 2024, [MNRAS](#), **531**, 183
- Nanni, A., Bressan, A., Marigo, P., & Girardi, L. 2013, [MNRAS](#), **434**, 2390
- Pardy, S. A., D’Onghia, E., & Fox, A. J. 2018, [ApJ](#), **857**, 101
- Pardy, S. A., D’Onghia, E., Navarro, J. F., et al. 2020, [MNRAS](#), **492**, 1543
- Pascale, R., Annibali, F., Tosi, M., et al. 2024, [A&A](#), **688**, A144
- Pastorelli, G., Marigo, P., Girardi, L., et al. 2020, [MNRAS](#), **498**, 3283
- Patel, E., Kallivayalil, N., Garavito-Camargo, N., et al. 2020, [ApJ](#), **893**, 121
- Pearson, S., Privon, G. C., Besla, G., et al. 2018, [MNRAS](#), **480**, 3069
- Peebles, P. J. E. 1982, [ApJL](#), **263**, L1
- Pilyugin, L. S., & Thuan, T. X. 2007, [ApJ](#), **669**, 299
- Rieke, G. H., Wright, G. S., Böker, T., et al. 2015, [PASP](#), **127**, 584
- Rieke, M. J., Kelly, D. M., Misselt, K., et al. 2023, [PASP](#), **135**, 028001
- Rousseau-Nepton, L., Martin, R. P., Robert, C., et al. 2019, [MNRAS](#), **489**, 5530
- Sabbi, E., Calzetti, D., Ubeda, L., et al. 2018, [ApJS](#), **235**, 23
- Sacchi, E., Annibali, F., Cignoni, M., et al. 2016, [ApJ](#), **830**, 3
- Sacchi, E., Bellazzini, M., Annibali, F., et al. 2024, [A&A](#), **691**, A65
- Salaris, M., & Cassisi, S. 1998, [MNRAS](#), **298**, 166
- Simon, J. D., & Geha, M. 2007, [ApJ](#), **670**, 313
- Smith, B. J., Giroux, M. L., Struck, C., & Hancock, M. 2010, [AJ](#), **139**, 1212
- Taylor, M. B. 2005, in ASP Conf. Ser. 347, Astronomical Data Analysis Software and Systems XIV, ed. P. Shopbell, M. Britton, & R. Ebert (San Francisco, CA: ASP), 29
- Thronson, H. A., Hunter, D. A., Casey, S., Latter, W. B., & Harper, D. A. 1989, [ApJ](#), **339**, 803
- Tikhonov, N. A., Galazutdinova, O. A., & Lebedev, V. S. 2014, [AstL](#), **40**, 1
- Tolstoy, E., Hill, V., & Tosi, M. 2009, [ARA&A](#), **47**, 371
- Tulin, S., & Yu, H.-B. 2018, [PhR](#), **730**, 1
- Ventura, P., Dell’Aglì, F., Schneider, R., et al. 2014, [MNRAS](#), **439**, 977
- Ventura, P., Karakas, A., Dell’Aglì, F., García-Hernández, D. A., & Guzman-Ramirez, L. 2018, [MNRAS](#), **475**, 2282
- Virtanen, P., Gommers, R., Oliphant, T. E., et al. 2020, [NatMe](#), **17**, 261
- Weisz, D. R., McQuinn, K. B. W., Savino, A., et al. 2023, [ApJS](#), **268**, 15
- Weisz, D. R., Dolphin, A. E., Savino, A., et al. 2024, [ApJS](#), **271**, 47
- Wheeler, C., Oñorbe, J., Bullock, J. S., et al. 2015, [MNRAS](#), **453**, 1305
- White, S. D. M., & Frenk, C. S. 1991, [ApJ](#), **379**, 52
- White, S. D. M., & Rees, M. J. 1978, [MNRAS](#), **183**, 341
- Zhang, L.-Y., Zhao, Y., & Zhang, H.-X. 2024, [ApJ](#), **965**, 3